Monthly Notices
of the
ROYAL ASTRONOMICAL SOCIETY

MNRAS **446,** 1411–1423 (2015) doi:10.1093/mnras/stu2162

The old, metal-poor, anticentre open cluster Trumpler 5⋆

P. Donati,[1,2]† G. Cocozza,[1] A. Bragaglia,[1] E. Pancino,[1,3] T. Cantat-Gaudin,[4,5] R. Carrera[6,7] and M. Tosi[1]

[1]*INAF-Osservatorio Astronomico di Bologna, via Ranzani 1, I-40127 Bologna, Italy*
[2]*Dipartimento di Fisica e Astronomia, Università di Bologna, via Ranzani 1, I-40127 Bologna, Italy*
[3]*ASI Science Data Center, I-00044 Frascati, Italy*
[4]*Dipartimento di Fisica e Astronomia, Università di Padova, vicolo Osservatorio 3, I-35122 Padova, Italy*
[5]*INAF-Osservatorio Astronomico di Padova, vicolo Osservatorio 5, I-35122 Padova, Italy*
[6]*Instituto de Astrofísica de Canarias, E-3200 La Laguna, Tenerife, Spain*
[7]*Departamento de Astrofísica, Universidad de La Laguna, E-38205 La Laguna, Tenerife, Spain*

Accepted 2014 October 15. Received 2014 October 9; in original form 2014 August 12

ABSTRACT

As part of a long-term programme, we analyse the evolutionary status and properties of the old and populous open cluster Trumpler 5 (Tr 5), located in the Galactic anticentre direction, almost on the Galactic plane. Tr 5 was observed with Wide Field Imager@MPG/ESO Telescope using the Bessel U, B, and V filters. The cluster parameters have been obtained using the synthetic colour–magnitude diagram (CMD) method, i.e. the direct comparison of the observational CMD with a library of synthetic CMDs generated with different stellar evolution sets (Padova, FRANEC, and FST). Age, reddening, and distance are derived through the synthetic CMD method using stellar evolutionary models with subsolar metallicity ($Z = 0.004$ or $Z = 0.006$). Additional spectroscopic observations with Ultraviolet VLT Echelle Spectrograph@Very Large Telescope of three red clump stars of the cluster were used to determine more robustly the chemical properties of the cluster. Our analysis shows that Tr 5 has subsolar metallicity, with $[\mathrm{Fe/H}] = -0.403 \pm 0.006$ dex (derived from spectroscopy), age between 2.9 and 4 Gyr (the lower age is found using stellar models without core overshooting), reddening $E(B-V)$ in the range 0.60–0.66 mag complicated by a differential pattern (of the order of $\sim\pm0.1$ mag), and distance modulus $(m-M)_0 = 12.4 \pm 0.1$ mag.

Key words: stars: abundances – Hertzsprung–Russell and colour–magnitude diagrams – open clusters and associations: general – open clusters and associations: individual: Trumpler 5.

1 INTRODUCTION

Old open clusters (OCs) are ideal probes of the Galactic disc structure, formation, and chemical distribution (see e.g. Friel 1995; Bragaglia & Tosi 2006; Magrini et al. 2009; Pancino et al. 2010; Lépine et al. 2011). Old clusters are only ∼15 per cent of the whole population of more than 2100 known OCs (see Dias et al. 2002) and only ∼5 per cent are older than 2 Gyr. However, old OCs are particularly important to constrain the formation and evolution, both dynamical and chemical, of the Milky Way disc. Using a combination of photometry, spectroscopy, and models, OCs' fundamental parameters (age, distance, and metallicity) are relatively easy to determine. In the *Gaia* era OCs will retain their importance. In fact, *Gaia* will produce exquisitely precise distances and proper motions for (almost) all MW OCs. This will permit us, for instance, to isolate the true cluster members, producing the best templates of simple stellar populations of different ages (hence stellar masses) to be used as robust test of all details of stellar evolutionary models. In turn, this will produce the best age estimates and will permit to derive the fine details of the evolution of the disc.

In the BOCCE (Bologna Open Cluster Chemical Evolution) project (Bragaglia & Tosi 2006; Donati et al. 2014a, and references therein), we use both the comparison between observed colour–magnitude diagrams (CMD) and stellar evolutionary models and the analysis of high-resolution spectra of stars to infer the cluster properties. We present here our study of Trumpler 5 (Tr 5 hereafter), a massive, old OC in the anticentre direction ($l = 202\overset{\circ}{.}865$, $b = 1\overset{\circ}{.}050$; Dias et al. 2002 and web updates). Tr 5 is interesting because it is metal poor ($[\mathrm{Fe/H}] \leq -0.3$ dex, according both to photometric and spectroscopic measures) and located at a Galactocentric distance (R_{GC}) of 10–13 kpc where a transition from a radially decreasing metallicity to a flat(ter) distribution seems to be present (e.g. Yong, Carney & Friel 2012, and references therein).

⋆This work is based on observations made at the ESO telescopes under programmes 68.D-0212 and 074.D-0344.

† E-mail: paolo.donati4@unibo.it

As is often the case for OCs, the properties of Tr 5 (age, distance, reddening) as measured in the literature show a large dispersion (see table 1 in Kim, Kyeong & Sung 2009, for a comprehensive list of values prior to this paper), even if the most recent determinations seem to agree better. The first photographic photometry of Tr 5 by Dow & Hawarden (1970) did not reach the main-sequence (MS) turn-off (TO), but already showed that the cluster is rich, old, and located in a highly (and differentially) reddened region. Kaluzny (1998, K98 hereafter) obtained CCD *BVI* photometry with the 0.9 m and 2.1 m telescopes on Kitt Peak; his data show a very well defined MS, a red giant branch (RGB), and an elongated red clump (RC). By comparing Tr 5 to M67, K98 found it only slightly younger. His distance modulus was $(m - M)_0 = 12.4$ mag and the reddening is $E(B - V) = 0.58$ mag, assuming solar metallicity. K98 found Tr 5 to be very massive (at least 3000 $M_\odot$). Using Kaluzny's data but fitting them with isochrones, Kim & Sung (2003) found a younger age (2.4 Gyr), a consistent distance modulus and reddening (12.64 mag and 0.64 mag, respectively), and [Fe/H] = −0.30 dex. Piatti, Clariá & Ahumada (2004, P04 hereafter), on the basis of VI_C and Washington photometry obtained with the 0.9 m telescope at Cerro Tololo and comparison with theoretical isochrones, determined rather different results for age (5 Gyr) and distance ($(m - M)_V = 13.8$ mag), while agreeing with past studies on reddening ($E(V - I) = 0.80$ mag, i.e. $E(B - V) = 0.64$ mag) and metallicity. They also determined a differential reddening ($\Delta E(B - V) = 0.11 - 0.22$ mag) and measured a cluster radius of about 7.7 arcmin. Finally, Kim et al. (2009) used the infrared 2 Micron All Sky Survey (2MASS) data and stellar isochrones to determine an age of 2.8 Gyr, an average reddening $E(B - V) = 0.64$ mag, a distance modulus $(m - M)_0 = 12.64$ mag, and [Fe/H] = −0.4 dex.

The metallicity of Tr 5 seems to be the least controversial parameter, since all studies agree on a subsolar value. This is confirmed by spectroscopy. Two independent studies employed the infrared calcium triplet (CaT). Cole et al. (2004) used a set of globular clusters (GCs) and OCs to calibrate the CaT method on literature data and applied the derived calibration to Tr 5, for which they obtained spectra of 16 stars (14 of which are RV members, with an average value of 54 ± 5 km s^{-1}). They obtained [Fe/H] = −0.56 ± 0.11 dex, making Tr 5 one of the metal-poorer known OC. This value was revised upwards by Carrera et al. (2007), who found instead [Fe/H] = −0.36 ± 0.05 dex, from the spectra of 17 member stars (average velocity 44 ± 10 km s^{-1}) and their CaT metallicity calibration based on many GCs and OCs. Finally, in a paper dedicated to the analysis of one lithium-rich evolved star, Monaco et al. (2014) found [Fe/H] = −0.49 (rms 0.04) dex from four giants observed with the UVES-FLAMES and MIKE spectrographs.

We present here our results obtained with the synthetic CMD technique for age, distance, and reddening and with the analysis of high-resolution spectra for metallicity and elemental abundances. The paper is organized as follows. The photometric and spectroscopic observations are described in Section 2, the spectroscopic analysis is illustrated in Section 3. Section 4 is dedicated to the photometric analysis of the cluster evolutionary properties. Summary and conclusions are in Section 5.

2 OBSERVATIONS AND DATA ANALYSIS

2.1 Imaging observations

Observations of Tr 5 were performed with the Wide Field Imager (WFI) mounted at the 2.2-m MPG/ESO Telescope of the La Silla Observatory (Chile), in 2001 November. The WFI instrument is a mosaic composed by two rows of four EEV CCDs (2096×4098 pixels) with a total field of view (FoV) of the instrument of 34×33 arcmin^2, with a pixel scale of 0.238 arcsec pixel^{-1}.

The data set consists of one long and two short exposures in each of the *U*, *B*, and *V* filters. The logbook of the observation is given in Table 1. The seeing was better than 1.3 arcsec for all the images. In Fig. 1 (produced with Aladin, Bonnarel et al. 2000), we show a Digitized Sky Survey (DSS) image of our field, with the eight WFI CCDs indicated. The cluster is almost entirely located in Chip #2 of the mosaic. One external field was also observed, in order to take into account the background/foreground contamination, pointing the telescope 50 arcmin south of the cluster centre. The standard

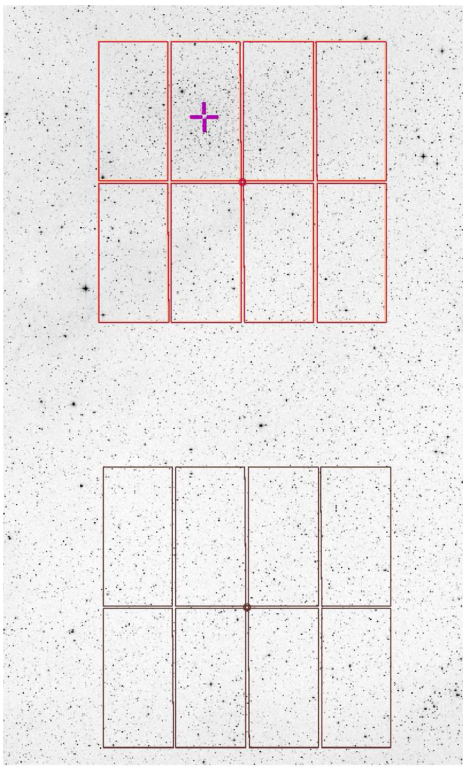

Figure 1. DSS image with the footprint of the WFI FoV for Tr 5 (upper) and the comparison field (lower). CCD #1 is the upper, leftmost; CCD numeration is clockwise. The cluster centre is indicated by a cross on CCD #2. North is up, east is left.

Table 1. Logbook of the WFI observations (RA and Dec refer to the centre of the telescope pointings).

Name	RA (h m s) J2000	Dec (° ′ ″) J2000	UT date	*U* Exp. time (s)	*B* Exp. time (s)	*V* Exp. time (s)	Seeing (arcsec)
Tr 5	6 36 16	9 22 50	25 Nov 2001	10; 600	3; 600	3; 600	0.9–1.3
Tr 5 ext	6 36 16	8 32 50	25 Nov 2001	10; 600	3; 600	3; 600	0.9–1.3

field SA92 (Landolt 1992) was also observed for photometric calibration, but the night was probably not photometric due to thin veils scattered all over the sky (see below for the calibration to the standard system).

2.2 Imaging data reduction

The raw WFI images were corrected for bias and flat-field, by using the standard package MSCRED included in IRAF.[1] The source detection and the instrumental magnitudes were performed independently for each *U*, *B*, and *V* frame and for each CCD of the WFI mosaic, using the point spread function (PSF) fitting code DAOPHOT II/ALLSTAR (Stetson 1987, 1993). For each CCD, a selected sample (120–170) of bright and well-isolated stars was adopted to compute the PSF in each exposure. In order to minimize geometrical distortions, which are present in the WFI mosaic, we used a spatially variable PSF, with a quadratic dependence on both *x* and *y* coordinates. We used the 2MASS Catalogue (Skrutskie et al. 2006) to compute the astrometric solution and transform the instrumental pixel coordinates into J2000 celestial coordinates. More than 2000 2MASS stars were used as astrometric standards, and cross-correlated with our catalogue using the CATAXCORR code,[2] developed by P. Montegriffo and widely used by our group in the past 10 years. The root-mean-square (rms) scatter of the solution was ∼0.1 arcsec in both RA and Dec.

In order to derive the completeness level of our photometry, we used the procedure successfully adopted in several previous studies by our group (e.g. Donati et al. 2012, for a description). About ∼250 000 stars have been artificially created and added uniformly in the deepest frames, in groups of ∼900 stars at each step, thus mimicking the addition of one single star at each time and avoiding any impact on the actual crowding condition. The instrumental magnitudes of all the artificial stars have been recovered using the same strategy described above, computing the completeness level of our photometry as the fraction of stars recovered for each magnitude interval. The result is shown in Table 2 but only for the *B* and *V* magnitudes, the two passbands we were able to calibrate (see the next section).

Table 2. Completeness of our photometry expressed in percentage. For magnitudes brighter than 16, completeness is 100 per cent.

mag	compl *B*	compl *V*
16.0	100 ± 0.1	100 ± 0.1
16.5	100 ± 0.1	99 ± 0.2
17.0	100 ± 0.1	98 ± 0.2
17.5	100 ± 0.2	98 ± 0.3
18.0	98 ± 0.3	98 ± 0.4
18.5	98 ± 0.3	97 ± 0.5
19.0	98 ± 0.4	97 ± 0.7
19.5	97 ± 0.6	95 ± 1.0
20.0	97 ± 0.8	95 ± 1.4
20.5	96 ± 1.1	93 ± 2.1
21.0	95 ± 2.5	83 ± 3.2
21.5	95 ± 2.2	65 ± 5.0
22.0	93 ± 3.2	41 ± 7.0
22.5	86 ± 4.6	12 ± 10.4
23.0	74 ± 6.9	2 ± 13.3
23.5	63 ± 10.6	
24.0	50 ± 16.0	
24.5	28 ± 23.2	
25.0	07 ± 30.1	
25.5	01 ± 33.6	

2.3 Photometric calibration

We intended to tie our instrumental magnitudes to the Johnson–Cousins photometric system using the observations of photometric standard stars. However, we encountered problems, due to both the non-photometric conditions during the observations and the paucity of standard stars in each single CCD, which forced us to use one single calibration equation for the whole mosaic in each filter. In fact, a comparison with photometric catalogues available in the literature (K98, P04) clearly exhibited systematic differences of our preliminary calibration varying from CCD to CCD (differences up to 0.5 mag in the $B - V$ colour). We supposed that this could be due to the well-known illumination problem of WFI, which was investigated by Koch et al. (2003). We therefore followed their same approach to correct the instrumental magnitudes for this effect but found that the overall correction was within ±0.1 mag in colour, too small with respect to the systematic differences we had from CCD to CCD. We concluded that in our case the illumination was only part of the problem and that we really needed a calibration equation for each CCD.

Therefore, we used the photometric catalogue of the stars observed by the Sloan Digital Sky Survey (SDSS) as a sort of secondary standards to obtain an independent calibration equation for each of the eight CCDs, and we transformed the SDSS magnitudes to the Johnson–Cousins system.[3] The same procedure was also applied to the external field. Unfortunately, it was possible to calibrate only the *B* and *V* images and not the *U* data because there are no transformations available for this passband. The calibration equations used for the FoV centred on the cluster are summarized in Table 3; the comparisons with the original SDSS catalogue are shown in Fig. 2 for CCD #2. For this CCD, in particular, we corrected the calibration of the *B* magnitude with a second iteration because a colour term was still present in the comparison with the SDSS catalogue (this occurrence did not show up for the external field).

The final catalogue contains *B* and *V* Johnson–Cousins magnitudes for 39 660 objects and is made available through the Centre de Données de Strasbourg (CDS)[4] and the web data base WEBDA.[5]

2.4 Comparison with previous data

Tr 5 was previously studied by many authors, as mentioned in Section 1. In particular, the photometric catalogues derived by K98 and by P04 are available in the WEBDA.

Of the three data sets in K98 (the first using the *V*, *I* filters, and the others using the *B*, *V* filters, see his Table 1), we decided to use for

[1] IRAF is the Image Reduction and Analysis Facility, distributed by the National Optical Astronomy Observatory, which is operated by the Association of Universities for Research in Astronomy (AURA) under cooperative agreement with the National Science Foundation.
[2] http://davide2.bo.astro.it/∼paolo/Main/CataPack.html

[3] For the conversion we used the equations available at http://www.sdss.org/dr4/algorithms/sdssUBVRITransform.html#Lupton2005
[4] http://cdsarc.u-strasbg.fr/viz-bin/qcat?J/MNRAS/
[5] http://webda.physics.muni.cz

Table 3. Calibration equations obtained for the eight CCDs for the Tr 5 pointing.

Equation	rms	Stars used
CCD 1		
$B - b = 24.576 + 0.253 \times (b - v)$	rms 0.01	About 1000
$V - v = 24.010 - 0.053 \times (b - v)$	rms 0.04	About 1200
CCD 2[a]		
$B - b = 24.533 + 0.355 \times (b - v)$	rms 0.04	About 1000
$V - v = 24.026 - 0.110 \times (b - v)$	rms 0.03	About 1200
CCD 3		
$B - b = 24.511 + 0.312 \times (b - v)$	rms 0.04	About 1600
$V - v = 24.016 - 0.080 \times (b - v)$	rms 0.04	About 2000
CCD 4		
$B - b = 24.534 + 0.316 \times (b - v)$	rms 0.05	About 1000
$V - v = 24.010 - 0.001 \times (b - v)$	rms 0.03	About 1000
CCD 5		
$B - b = 24.564 + 0.278 \times (b - v)$	rms 0.04	About 1000
$V - v = 24.021 - 0.115 \times (b - v)$	rms 0.04	About 1200
CCD 6		
$B - b = 24.504 + 0.387 \times (b - v)$	rms 0.04	About 1000
$V - v = 23.961 - 0.042 \times (b - v)$	rms 0.03	About 1600
CCD 7		
$B - b = 24.496 + 0.379 \times (b - v)$	rms 0.05	About 1000
$V - v = 23.953 - 0.053 \times (b - v)$	rms 0.04	About 1400
CCD 8		
$B - b = 24.545 + 0.272 \times (b - v)$	rms 0.04	About 800
$V - v = 23.975 - 0.070 \times (b - v)$	rms 0.03	About 1000

[a] B magnitude obtained from this equation is then corrected to compensate for a colour term using the following equation: $B^{\star} = -0.012 \times B + 0.237$.

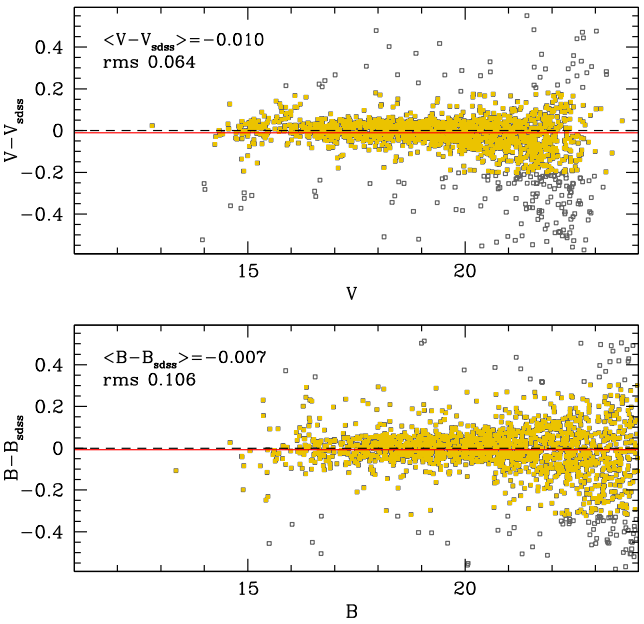

Figure 2. Comparison of the calibrated B and V magnitudes with the SDSS photometry for CCD #2. The yellow-filled dots are the stars used to compute the mean difference within 2σ from the average. The differences are compatible with 0, without trends with magnitude. The same conclusions apply to all the other CCDs of the instrument.

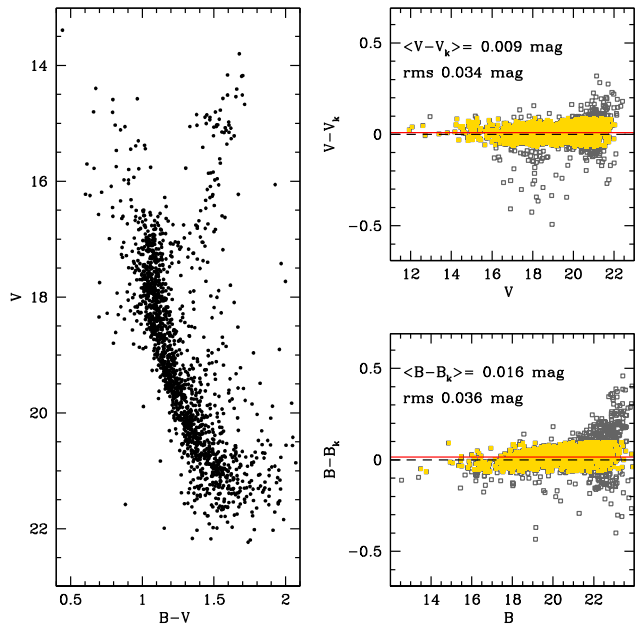

Figure 3. Left-hand panel: CMD of Tr 5 in the V, BV plane from run 2 by K98. Right-hand panels: differences between our photometry and the K98 one in V (upper panel) and B (bottom panel). The points in the right-hand panels show the data for all the stars in common, while the yellow-filled dots are the stars used to compute the mean difference within 2σ from the average.

the comparison with our photometry only the second run, obtained in better conditions and with a better instrument. Moreover, the FoV of this data set nicely matches the FoV of CCD #2 of the WFI instrument, which includes almost completely Tr 5. In Fig. 3, we show the differences between our photometry and the photometry by K98. In general, B and V compare well; differences are within 0.02 mag with a mild dependence on magnitude, especially in B. Our bright stars are in general slightly bluer than in K98. This is probably due to the fact that the B filter mounted on the WFI instrument differs from the classical B filter in the Johnson–Cousins system used by K98.

In the case of P04 (see Fig. 4), only the V magnitude can be compared. We found an average difference of $\langle V - V_P \rangle = 0.035$ mag, larger than the difference found with the V of K98 but with no evident trend with magnitude.

We deemed both comparisons acceptable and took them as an indication of the validity of our calibration on the SDSS data.

2.5 Cluster centre and CMD

Exploiting the deep and precise photometry obtained with WFI and its large FoV, we re-determined the centre of the cluster following the approach described in Donati et al. (2012). Briefly, we selected the densest region on the images by looking for the smallest coordinates interval that contains 70 per cent of all the stars. The centre is obtained as the average right ascension and declination when the selection is iterated twice. For a more robust estimate, several magnitude cuts have been considered and the corresponding results averaged. The rms on the centre coordinates is about 2 arcsec. We found RA(J2000) = 06:36:28.22, Dec(J2000) = +09:28:04.26,

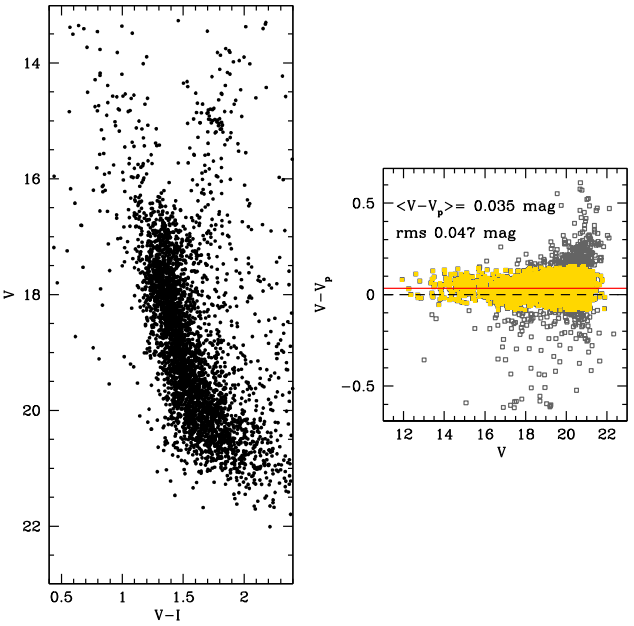

Figure 4. Left-hand panel: CMD of Tr 5 in the *V*, *VI* plane from P04. Right-hand panel: differences between our photometry and the P04 one in *V*.

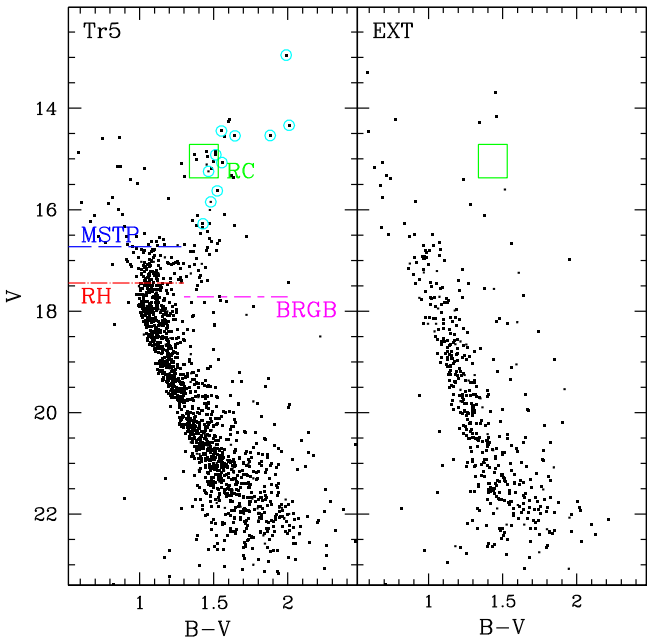

Figure 5. Left-hand panel: CMD for stars inside 3 arcmin from the cluster centre; the open circles are the RV candidate members (from the literature, see Table 4) together with our spectroscopic targets (see the next sections) located inside this radius. Right-hand panel: external field of the same area. We highlight the RC locus in both CMDs and the main evolutionary phases of the cluster in the left-hand panel.

significantly different from the values cited in WEBDA (RA = 06:36:42, Dec = +09:26:00 both referred to J2000). From the density profile, it was also possible to define the apparent diameter of the cluster. We estimated $d = 26$ arcmin $\pm$ 4 arcmin using the radius at which the density profile flattens at the background density value; the cluster appears larger than found by P04, probably thanks to the advantage of a wider FoV.

With this information, we analysed the morphology of the cluster CMD. As apparent from Fig. 5, where we show Tr 5 and the comparison field, the cluster is populous. The MS is well visible, as is the rich RC. The high contamination by field objects clearly complicates the interpretation of the evolutionary features, especially the red-hook (RH, the reddest point on the MS before the overall contraction), the MS termination point (MSTP, the most luminous level of the MS phase before the runaway to the red), and the RGB. By considering only the innermost part of the cluster, it is possible to minimize the pollution of field interlopers. Furthermore, we can use information on membership from spectroscopy. Table 4 lists the stars in common in our photometry and published spectroscopic studies, which are also shown in Fig. 5 (left-hand panel) as large open circles. In Fig. 6, we show the CMDs of Tr 5 for different distances from the cluster centre (from left to right: 1, 2, 3 arcmin). We used the radial plots to identify the evolutionary features of the cluster employed in the following analysis (see Section 4), and we identified:

(i) the RC at $V \sim 15$ mag and $(B - V) \sim 1.55$ mag;
(ii) an extended RGB, with the base of the RGB (BRGB) at $V \sim 17.4$ mag;
(iii) the MSTP at $V \sim 16.8$ mag and the blue edge (BE) of the MS at $(B - V) \sim 1$ mag;
(iv) the RH at $V \sim 17.3$ mag;
(v) and the MS extending down to $V \sim 23$ mag.

2.6 Differential reddening

The CMD of Tr 5 (see Figs 5 and 6) shows an MS which has a non-negligible extension in colour. Such broadening cannot be explained only by the photometric error, which is small especially at bright magnitudes. Apart from contamination by field stars, other possible influencing agents are the presence of binary systems, a spread in age or in metallicity, and differential reddening (DR). We exclude a large spread in age, which would not explain the evident broadening of the lower MS, or in metallicity, since no OC has ever convincingly been demonstrated to have it. Binarism, instead, has always been found in OCs, and indeed we do take it into account in the CMD analysis, but it leads to a smaller colour spread with a typical inclination with respect to the single star MS. DR seems the most plausible explanation because the patchy structure of dust intercepted along the line of sight has the net effect to shift the colour and magnitude of the stars along the reddening vector: the denser the interstellar medium the redder and fainter the observed colour and magnitude. This condition is particularly likely for objects residing on the disc and with a high average reddening, as is the case of Tr 5 ($b \sim 1^\circ$, $E(B - V) \sim 0.6$). Furthermore, Tr 5 lies in the vicinity of the star forming region NGC 2264 and of the Cone nebula. Tr 5 is not a peculiar case. In fact, non-negligible DR has been found in many other clusters (see e.g. Brogaard et al. 2012; Platais et al. 2012; Donati et al. 2014a,b, only to name a few cases).

To quantify the effect of DR, we use a method based on the one described by Milone et al. (2012), but adapted to the case of OCs. As explained in more details in Donati et al. (2014a,b), we use stars selected within a region on the MS and in small spatial areas (here, 50 arcsec × 50 arcsec) and compute their average distance along the reddening vector from a fiducial line (i.e. their DR). We evaluated the DR only inside 4 arcmin from the cluster centre, where the density of stars is about 50 per cent higher than in the

Table 4. Stars in common between our photometry and CaT spectroscopy (RV_{04} from Cole et al. 2004, RV_{07} from Carrera et al. 2007) and FLAMES spectra (RV_{UV}; Monaco et al. 2014).

ID	Other (WEBDA)	RA (h:m:s)	Dec (d:′:′′)	B	V	RV_{04} (km s^{-1})	RV_{07} (km s^{-1})	RV_{UV} (km s^{-1})	Notes
100016	1318	6:36:53.47	+09:25:34.6	16.495	15.099	–	–	48.1	
200008	1063	6:36:24.23	+09:25:15.3	16.418	14.537	–	51.8	–	
200015	4791	6:36:33.15	+09:33:03.7	16.500	15.002	–	–	50.0	
200027	2565	6:36:28.48	+09:28:13.4	17.326	15.846	60.5	–	–	
200070	1834	6:36:35.56	+09:26:48.0	17.706	16.278	50.8	–	–	
200113	488	6:36:40.41	+09:23:45.1	18.294	16.557	57.1	–	–	
204788	833	6:36:42.07	+09:24:34.2	16.696	14.998	54.4	39.8	–	
204791	3416	6:36:40.20	+09:29:47.8	16.521	15.062	–	–	49.8	
204801	2280	6:36:35.99	+09:27:35.2	16.709	15.244	47.8	35.9	–	
204816	1401	6:36:28.10	+09:25:56.3	16.650	15.349	14.8	–	–	NM
204823	2324	6:36:24.83	+09:27:46.6	16.627	15.072	53.1	41.6	–	
204826	2579	6:36:23.93	+09:28:17.2	17.153	15.629	47.8	40.9	–	
204847	5099	6:36:18.81	+09:34:06.6	14.459	12.352	–	48.7	–	
204849	4219	6:36:23.44	+09:31:37.7	14.857	12.598	–	31.4	–	
204851	1935	6:36:33.12	+09:27:00.9	14.941	12.952	53.5	45.9	–	
204856	1378	6:36:19.26	+09:25:58.7	15.360	13.414	–	42.9	–	
204859	4811	6:36:47.32	+09:32:59.6	15.421	13.734	–	54.0	–	
204864	1214	6:36:42.29	+09:25:25.7	15.704	14.014	55.7	34.4	–	
204871	1305	6:36:24.54	+09:25:46.7	16.345	14.336	64.9	61.0	–	
204873	3066	6:36:36.47	+09:29:08.1	16.000	14.448	50.7	37.7	–	
204876	3354	6:36:29.31	+09:29:45.2	16.188	14.544	53.7	29.2	–	
204877	3763	6:36:34.11	+09:30:34.6	16.138	14.566	−3.9	−20.6	–	NM
204885	1026	6:36:42.96	+09:25:02.3	16.428	14.823	–	29.7	–	
204896	4649	6:36:48.04	+09:32:33.5	16.602	14.999	–	–	47.3	NM
–	6223	6:36:38.6	+09:38:52.6	16.57	15.08	–	–	50.8	

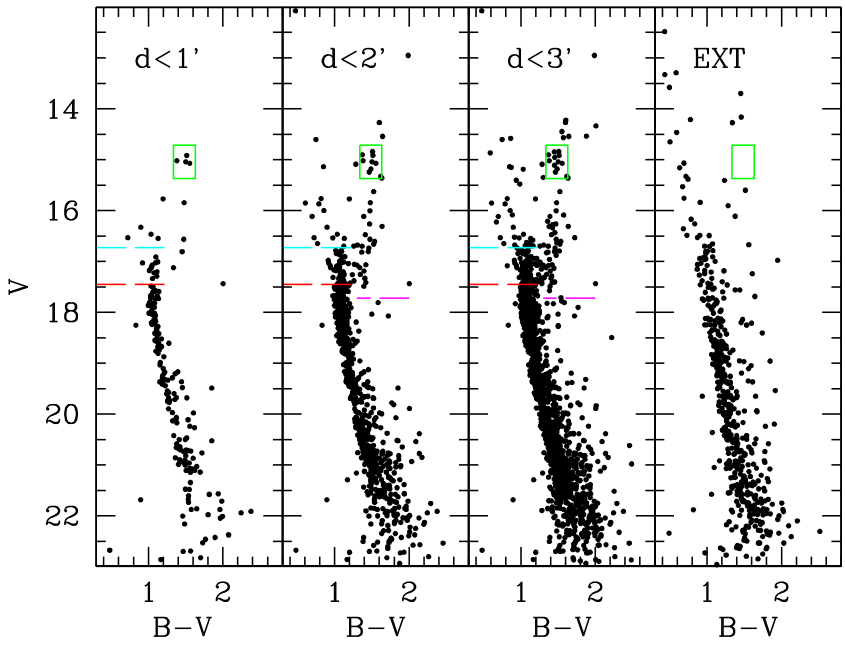

Figure 6. CMDs for different distances from the cluster centre (first three panels from left to right: $d < 1$ arcmin, $d < 2$ arcmin, and $d < 3$ arcmin), compared with an external field of a circular area of 3 arcmin radius. We highlight the main evolutionary phases: RH, MSTP, and RC. For a better comparison the RC box is also shown in the CMD of the external field.

external region of our FoV. We avoided the external parts, where our estimation of DR could be severely jeopardised by the presence of too many field interlopers. The resulting DR map and the map of the error on the average are shown in Fig. 7.

The DR ranges between about −0.1 and +0.15. The standard deviations of the DR measurements in each cell of the grid range from less than 0.01 mag up to 0.07 mag, with an average of 0.02 mag. This strong variation within the same spatial cell of the grid are in part due to the intrinsic variation of the reddening on the cluster face coupled with the strong contamination of field interlopers. The combination of these two factors limits the precision of the DR measurements and translates into errors on the average values

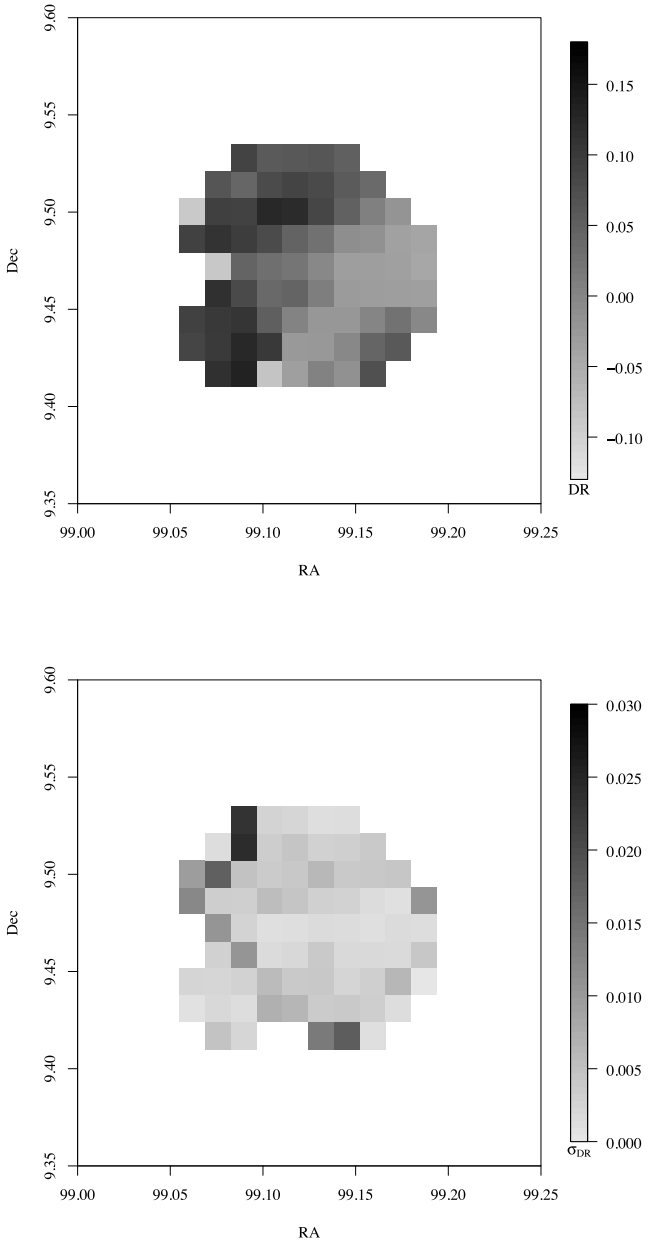

Figure 7. These plots show the reddening map (upper panel) and the corresponding error (lower panel) in RA and Dec (expressed in degrees) obtained for Tr 5. The spatial resolution used is 50 arcsec × 50 arcsec. The colour code indicates where DR (upper panel) and the error (lower panel) are stronger (dark colour) or weaker (light colour).

within each cell up to 0.03 mag in the worst case. In Fig. 8, we show the comparison between the CMDs with and without the correction for DR. The MS appears considerably improved, with a much tighter extension in colour; also the giant phases seem to be much better defined, in particular the SGB, RGB, and the RC. The sequence of binaries is much more evident after the correction and it still contributes to the spread of the MS. Their impact on the CMD appearance is quantified using the synthetic CMD method (see Section 4).

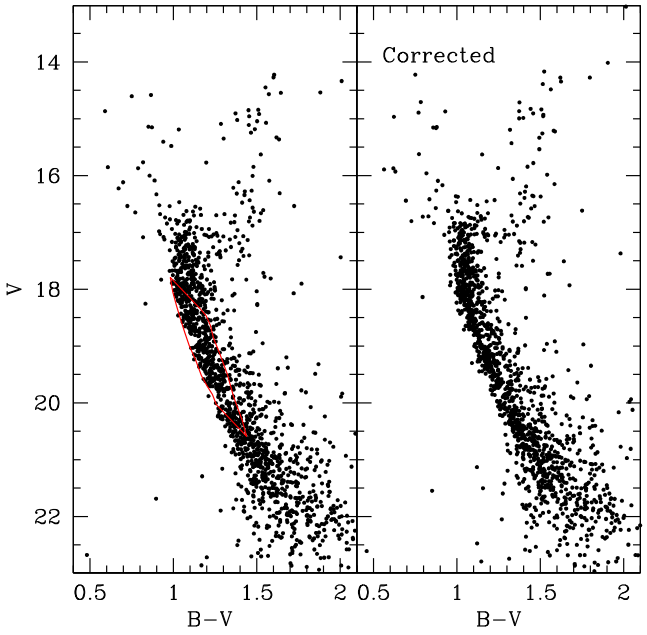

Figure 8. On the left: the observed CMD within 3 arcmin, with the red curve enclosing the MS portion used to estimate the DR effect. On the right: the CMD on the same region after the correction for the resulting DR.

2.7 Spectroscopy observations and reductions

The spectra of three RC stars were acquired in service mode at the ESO Very Large Telescope (VLT) with the high-resolution spectrograph UVES (Ultraviolet VLT Echelle Spectrograph; D'Odorico et al. 2000). None of them is in common with the samples of Cole et al. (2004), Carrera et al. (2007), and Monaco et al. (2014) but all three are cluster members, according to their radial velocity (RV, see below). Details of the observations are given in Table 5, where airmass and seeing are approximate average values for the three spectra in each night. We employed a slit width of 1.2 arcsec ($R \simeq 40\,000$) and the dichroic, that splits the light into a blue channel (CD#2, λλ 3280–4560 Å) and a red channel (CD#3, λλ 4720–5800, 5810–6830 Å).

We used the spectra reduced (extracted, wavelength calibrated, and sky subtracted) by ESO and retrieved from the ESO Advanced Data Products archive. Individual spectra have signal-to-noise (S/N) less than 10 in the blue chip, about 25 in the lower chip of the red channel, and about 35 in the upper chip. We discarded the blue spectra and averaged (using the median) the individual red spectra for each star using IRAF: the S/N of the combined spectra in the lower and upper red channels are reported in Table 6.

We measured the equivalent widths (EWs) of atomic lines in the combined spectra using DOOp (Cantat-Gaudin et al. 2014), an automated wrapper for DAOSPEC (Stetson & Pancino 2008), originally devised for the analysis of the many thousands of spectra obtained by the *Gaia*-ESO Survey (see Gilmore et al. 2012; Randich et al. 2013,

Table 5. Log of the UVES observations.

ID	Other (WEBDA)	Date obs (UT)	Exptime (s)	Seeing (arcsec)	Airmass
204893	2604	2005-01-04	3×860	2.8	1.50
		2005-01-05	3×860	1.2	1.23
204783	3236	2005-01-08	3×960	0.9	1.21
204892	2553	2005-02-12	3×860	1.0	1.23

Table 6. Photometry, coordinates at J2000.0, RV, S/N in the lower and upper CCDs, and atmospheric parameters of the three stars observed with UVES.

ID	B	V	K (2MASS)	RA (h:m:s)	Dec (d:′:″)	RV (km s^{-1})	S/N (lower)	S/N (upper)	$T_{\rm eff}$ (K)	log g	v_t (km s^{-1})	[Fe/H]
204892	16.431	14.917	10.588	6:36:31.24	+09:28:10.9	51.8 ± 1.1	30	55	4750	2.60	1.40	–0.40
204893	16.316	14.933	11.018	6:36:41.94	+09:28:11.7	49.2 ± 1.0	45	70	5000	2.70	1.70	–0.41
204783	16.690	15.223	11.134	6:36:44.06	+09:29:23.5	48.1 ± 0.9	35	60	4850	2.80	1.30	–0.40

Table 7. Equivalent widths of the used atomic species. Only the first few lines are reproduced here, the complete table can be found in its electronic form at CDS.

ID	λ (Å)	Species	$\chi_{\rm ex}$ (eV)	loggf (dex)	EW (mÅ)	δEW (mÅ)	Q
204893	4808.148	Fe I	3.250	−2.690	45.60	2.66	0.837
204893	4809.938	Fe I	3.570	−2.620	22.50	2.04	0.868
204893	4873.751	Fe I	3.300	−2.960	28.90	3.18	1.340
204893	4874.353	Fe I	3.070	−3.088	36.10	2.56	0.938
204893	4896.439	Fe I	3.880	−1.950	45.40	1.76	0.522

for a description). The line list employed was prepared for the *Gaia*-ESO Survey (by the line list group; Heiter et al., in preparation) and is based on VALD3 (Ryabchikova, Pakhomov & Piskunov 2011) atomic data. The measured EWs and their errors, the excitation potentials and log gf values of the transitions, and the DAOSPEC quality parameter for each line can be found in Table 7 (available in its entirety only in electronic form).

The observed RV is an output of DAOSPEC,[6] and telluric absorption features were used to correct for any wavelength calibration shifts or misalignments within the slit, following the procedure described by Pancino et al. (2010). Heliocentric corrections were applied and the resulting heliocentric RVs are listed in Table 6, together with coordinates, magnitudes, and atmospheric parameters (see Section 3).

3 ABUNDANCE ANALYSIS

Abundances and atmospheric parameters were derived with GALA (Mucciarelli et al. 2013), an automated wrapper for the Kurucz abundance calculation code (Sbordone et al. 2004; Kurucz 2005), employing Atlas atmospheric models[7] (based on the grid by Castelli & Kurucz 2003). GALA uses the classical EW method, where initial first guesses of the atmospheric parameters are refined by erasing trends of Fe abundance with the excitation potential (to refine $T_{\rm eff}$), with EW (to refine v_t), and with wavelength (as a general sanity check of the method). Surface gravity is refined by imposing ionization balance, i.e. that Fe I and Fe II give the same Fe abundance, within the uncertainties. Initial guesses for the atmospheric parameters were obtained from stellar models and our experience with subsolar metallicity RC stars ($T_{\rm eff} \simeq 5000$ K, log $g \simeq 2.5$ dex, $v_t \simeq 1$ km s^{-1}) and GALA was let free to seek for convergence starting from there: the final, adopted parameters are listed in Table 6. We found an average metallicity [Fe/H] = −0.40 dex, based on ≃170 Fe I lines and ≃20 Fe II lines, confirming that Tr 5 is a metal-poor OC. Its position in the Galactic disc metallicity distribution will be discussed in Section 5.

We also measured abundances for the light elements Al (based on two or three lines, depending on the star) and Na (3 lines); the α-elements Ca (≃9 lines), Mg (3 lines), Si (≃22 lines), and Ti (≃50 Ti I and ≃10 Ti II lines); the iron-peak elements Sc (≃3 Sc I and ≃10 Sc II lines), V (≃25 lines), Cr (≃22 lines), Co (≃20 lines), and Ni (≃53 lines); and the heavy elements La (2 lines), Pr (2 lines), Nd (≃19 lines), and Y (≃7 lines). All our abundances were derived in LTE (local thermodynamic equilibrium) and without corrections for HFS (hyper fine structure) effects. Abundances of the species listed in Table 8 were derived as the weighted average of the abundances provided by the single lines, with their error, computed as the sigma on the weighted average, divided by the square root of the number of used lines. The adopted solar composition was the one by Grevesse, Noels & Sauval (1996).

The uncertainty owing to the continuum placement was between 2 and 5 per cent judging from the DAOSPEC residuals after removal of the fitted lines; globally this corresponds to approximately an error of 5–10 mÅ on the single lines, that can amount to approximately 0.05 dex at most in the [Fe/H] abundance, for example. The additional uncertainty implied by the choice of atmospheric parameters was estimated using the Cayrel et al. (2004) method, which takes automatically into account correlations among the parameters by altering just one of them (in our case $T_{\rm eff}$, by ±100 K) and keeping it fixed to a wrong value, while re-optimizing the other parameters. The resulting uncertainties are reported in Table 8 between parenthesis.

Most abundance ratios appear solar within the uncertainties, although Mg, Al, Pr, Nd, and La are slightly supersolar as seen in other OCs of similar metallicity (Bragaglia et al. 2008; Sestito et al. 2008; Pancino et al. 2010; Carrera & Pancino 2011; Yong et al. 2012). The three stars share a very homogeneous composition in all the examined species; this conclusion is robust even if we did not correct for departure from LTE or HFS, since they are in the same evolutionary status and their atmospheric parameters are essentially identical.

Very similar conclusions can be reached using the results published in Monaco et al. (2014). That paper is devoted to the analysis of a Li-rich RC star and the properties of the normal stars are not discussed, so we cannot make a detailed comparison here. However, from the tables in their appendix we see that the four stars that they consider member of Tr 5 (all in the RC phase) have properties similar to the ones we derived for our three stars. In particular, we find ⟨RV⟩ = 49.7 (rms 1.9) km s^{-1}, while they have ⟨RV⟩ = 49.8 (rms 1.1) km s^{-1}, the average metallicities are −0.40 and −0.49 dex, respectively, and we also have similar abundances for the elements in common. Finally, also in their analysis the stars show a very homogeneous composition, without any anomalous spread.

[6] As shown in Table 5, the spectra of each star were taken consecutively, hence RVs were measured on the averaged spectra given that there were no significant shifts in wavelength from spectrum to spectrum.

[7] GALA allows for a quick computation with both the Atlas and the MARCS (Gustafsson et al. 2008) atmospheric models. The use of MARCS models provides almost identical results: ⟨Δ$T_{\rm eff}$⟩ = +17 K, ⟨Δlog g⟩ = −0.1 dex, ⟨Δv_t⟩ = −0.03 km s^{-1}, ⟨Δ[Fe/H]⟩ = +0.01 dex, with all differences computed in the sense MARCS minus Atlas.

Table 8. Abundance ratios (with respect to neutral iron), with internal errors ($\sigma/\sqrt{(\mathrm{nlines})}$) and sensitivity of each abundance to changes in atmospheric parameters between parenthesis (see the text). The cluster average and sigma are also indicated, along with the solar reference abundance (see the text).

Ratios	Star 204892 (dex)	Star 204893 (dex)	Star 204783 (dex)	Tr 5 (dex)	Sun
[Fe I/H]	-0.40 ± 0.01 (± 0.06)	-0.41 ± 0.01 (± 0.06)	-0.40 ± 0.01 (± 0.09)	-0.40 ± 0.01	7.50
[Fe II/H]	-0.44 ± 0.01 (± 0.09)	-0.42 ± 0.02 (± 0.03)	-0.36 ± 0.02 (± 0.08)	-0.41 ± 0.04	7.50
[Na I/Fe]	$+0.00 \pm 0.03$ (± 0.06)	-0.02 ± 0.06 (± 0.06)	$+0.05 \pm 0.05$ (± 0.08)	$+0.01 \pm 0.04$	6.33
[Mg I/Fe]	$+0.17 \pm 0.02$ (± 0.03)	$+0.20 \pm 0.03$ (± 0.06)	$+0.24 \pm 0.03$ (± 0.06)	$+0.20 \pm 0.04$	7.58
[Al I/Fe]	$+0.21 \pm 0.07$ (± 0.06)	$+0.20 \pm 0.04$ (± 0.06)	$+0.25 \pm 0.03$ (± 0.08)	$+0.22 \pm 0.03$	6.47
[Si I/Fe]	-0.02 ± 0.02 (± 0.03)	$+0.01 \pm 0.03$ (± 0.02)	$+0.05 \pm 0.03$ (± 0.03)	$+0.01 \pm 0.04$	7.55
[Ca I/Fe]	$+0.05 \pm 0.03$ (± 0.09)	$+0.05 \pm 0.02$ (± 0.08)	$+0.09 \pm 0.02$ (± 0.12)	$+0.06 \pm 0.02$	6.36
[Sc I/Fe]	-0.11 ± 0.03 (± 0.15)	-0.11 ± 0.07 (± 0.18)	-0.01 ± 0.03 (± 0.15)	-0.08 ± 0.06	3.17
[Sc II/Fe]	$+0.18 \pm 0.04$ (± 0.06)	$+0.20 \pm 0.04$ (± 0.08)	$+0.15 \pm 0.04$ (± 0.06)	$+0.18 \pm 0.03$	3.17
[Ti I/Fe]	-0.04 ± 0.01 (± 0.12)	-0.05 ± 0.01 (± 0.14)	$+0.02 \pm 0.01$ (± 0.15)	-0.02 ± 0.04	5.02
[Ti II/Fe]	$+0.12 \pm 0.03$ (± 0.08)	$+0.04 \pm 0.04$ (± 0.06)	$+0.08 \pm 0.02$ (± 0.06)	$+0.08 \pm 0.04$	5.02
[V I/Fe]	$+0.06 \pm 0.02$ (± 0.15)	-0.03 ± 0.02 (± 0.17)	$+0.08 \pm 0.03$ (± 0.18)	$+0.04 \pm 0.06$	4.00
[Cr I/Fe]	-0.08 ± 0.03 (± 0.09)	$+0.04 \pm 0.05$ (± 0.11)	-0.09 ± 0.03 (± 0.12)	-0.04 ± 0.07	5.67
[Co I/Fe]	$+0.11 \pm 0.03$ (± 0.09)	$+0.03 \pm 0.03$ (± 0.14)	$+0.10 \pm 0.03$ (± 0.11)	$+0.08 \pm 0.04$	4.92
[Ni I/Fe]	-0.07 ± 0.02 (± 0.05)	-0.06 ± 0.02 (± 0.06)	-0.05 ± 0.02 (± 0.08)	-0.06 ± 0.01	6.25
[Y II/Fe]	-0.08 ± 0.04 (± 0.06)	-0.07 ± 0.04 (± 0.09)	$+0.05 \pm 0.09$ (± 0.06)	-0.03 ± 0.07	2.24
[La II/Fe]	$+0.16 \pm 0.07$ (± 0.09)	$+0.10 \pm 0.06$ (± 0.14)	$+0.22 \pm 0.02$ (± 0.09)	$+0.16 \pm 0.06$	1.17
[Pr II/Fe]	$+0.29 \pm 0.17$ (± 0.08)	$+0.03 \pm 0.12$ (± 0.14)	$+0.15 \pm 0.12$ (± 0.09)	$+0.16 \pm 0.13$	0.71
[Nd II/Fe]	$+0.21 \pm 0.03$ (± 0.08)	$+0.19 \pm 0.03$ (± 0.12)	$+0.19 \pm 0.03$ (± 0.09)	$+0.20 \pm 0.01$	1.50

4 CLUSTERS PARAMETERS USING SYNTHETIC CMDs

The age, distance modulus, metallicity, reddening, DR, and binary fraction of the cluster are estimated using the synthetic CMD technique (see Tosi et al. 1991) as done in all the papers of the BOCCE project (see e.g. Cignoni et al. 2011; Donati et al. 2012, 2014a and references therein). For a detailed description, see Bragaglia & Tosi (2006). Briefly, we compute a grid of synthetic CMDs in the age–metallicity–distance–reddening space using three sets of stellar evolution models, i.e. the Padova (Bressan et al. 1993; Fagotto et al. 1994), the FRANEC (Dominguez et al. 1999), and the FST (Ventura et al. 1998) tracks, chosen to test the effect of different input physics on the derivation of cluster fundamental parameters. In fact, these models use different prescriptions for the treatment of convection, going from no overshooting (FRANEC), to the standard description of overshooting through parametrization of the mixing length (Padova), to overshooting treated using the so-called full spectrum of turbulence modellization (FST). The last models have also the possibility of choosing between three different levels of overshooting (none, moderate, and high). These tracks offer only a few possible metallicities, and we do not interpolate between them. In particular, the metallicity values we normally use for OCs are $Z = 0.02, 0.008, 0.004$ (Padova); $Z = 0.02, 0.01, 0.006$ (FRANEC); and $Z = 0.02, 0.006$ (FST). All these models are available only with one choice of helium and solar-scaled α elements. The lack of a fine metallicity grid and of different levels of α-enhancement prevents a direct comparison with the metallicity and chemical composition derived from the spectra. Although more modern tracks are available nowadays, we favour homogeneity of treatment and continue to use the same ones adopted throughout the BOCCE project.

For Tr 5 all synthetic CMDs are built assuming an approximately instantaneous star formation burst (5 Myr long) and using a single slope Salpeter initial mass function over the range in mass covered by the tracks. The photometric conversions from the theoretical effective temperature–luminosity plane to the empirical colour–magnitude plane are obtained with the same conversion tables (see Bessell, Castelli & Plez 1998) for all the sets of tracks. Cluster parameters are determined by means of the comparison of the synthetic CMDs with the observed ones. The best-fitting solution is chosen as the one that can best reproduce age-sensitive indicators (highlighted in Section 2.5): the RH, the RC, the MSTP, the BRGB, the RGB inclination and colour, and the RC colour. The latter two were used as secondary age indicators as colour properties are more affected by theoretical uncertainties, like colour transformation and superadiabatic convection, while luminosity constraints are more reliable.

Multicolour photometry has generally proved to be fundamental to obtain the best parameters estimation (see, e.g. Ahumada et al. 2013, for a discussion), especially metallicity. The best-fitting solutions must reproduce at the same time the observed CMDs in different colours for appropriate distance modulus, reddening, and age. However, for Tr 5 we knew from literature spectroscopy that the cluster is rather metal poor and we confirmed that with the UVES spectra. This helped us in restricting the possible range of evolutionary tracks. We used our *B*, *V* photometry for the synthetic CMD technique coupled with the P04 *V*, *I* photometry to help constraining the photometric metallicity.

We estimated the errors on the cluster parameters considering both the instrumental photometric errors and the uncertainties of the fit analysis, as done in Donati et al. (2012). The net effect of the former is an uncertainty on the luminosity level and colour of the adopted indicators. This affects mainly the estimate of the mean Galactic reddening and distance modulus, as they are directly defined by matching the level and colour of the upper MS and the RH and MSTP indicators. We must also consider the dispersion in the results arising from the fit analysis. Tr 5 is heavily contaminated, and the definition of important indicators, such as the RC locus or the MSTP, is more uncertain. Hence, we cannot find a unique solution, but only a restricted range of viable solutions. In practice, we select the best-fitting synthetic CMD and then take into account

the dispersion of the cluster parameters estimates in the error budget. The uncertainties are assumed to be of the form:

$$\sigma^2_{E(B-V)} \sim \sigma^2_{(B-V)} + \sigma^2_{\rm fit}$$

$$\sigma^2_{(m-M)_0} \sim \sigma^2_V + R^2_V \sigma^2_{E(B-V)} + \sigma^2_{\rm fit}$$

$$\sigma^2_{\rm age} \sim \sigma^2_{\rm fit}.$$

Typical photometric errors are ∼0.04 on the reddening and ∼0.1 on the distance modulus (assuming negligible the error on R_V). The error resulting from the fit analysis depends mainly on the uncertainty on the RC level and on the coarseness of the models grid. It is of the order of ∼0.02 for the reddening, ranges between 0.01 and 0.05 for the distance modulus, and is about 0.1 Gyr for the age.

4.1 CMD

As discussed in Section 2.6, the cluster's MS is much broader than expected from photometric errors. This is due to two factors: the presence of DR and a significant fraction of unresolved binaries. The former aspect is discussed and quantified in Section 2.6 and for our simulation we compared the synthetic CMDs with the observed CMD corrected for DR. For binaries, a rough estimate of their fraction was obtained following the method described in Cignoni et al. (2011): we defined two CMD boxes, one which encloses (the bluer) MS stars and the other redwards of the MS in order to cover the binary sequence. To remove the field contamination, we subtracted the contribution of field stars falling inside the same CMD boxes of an equal area of the control field. We performed the same computation on regions of different sizes, eventually ending up with an estimate between 20 and 35 per cent. The dispersion on the estimate is mostly due to the spatial fluctuations across the control field. These fractions are probably underestimated, since we are missing binaries hosting a low mass star, whose properties are close to those of single stars. We assumed a fraction of 25 per cent for all the simulations.

Even considering the correction for DR and binaries, we were not able to match the broadening of the MS with the synthetic CMD. We were forced to consider an additional random component of DR of the order of 0.07 mag. This value matches the largest dispersion we found in DR measurements, which, as explained in Section 2.6, are limited in precision due to the large intrinsic spatial variation of the DR across the cluster face and to the contamination of field interlopers.

The best solution for each set of tracks is the one whose synthetic CMD fits 'most' of the visible MS shape and the RC and MSTP luminosity levels. In general, we found RGB and RC colours slightly redder in the synthetic CMDs than in the observed one. These evolutionary stages depend on physical parameters like the metallicity, the age, the helium content as well as on more subtle physical assumptions like the efficiency of core overshooting and the amount of mass-loss during the pre-helium burning phase, see Castellani et al. (2000). Moreover, the synthetic colours of the coolest phases are also affected by the uncertainties in the photometric conversions. We found overall good agreement for the other evolutionary phases. Among the metallicity range allowed by the evolutionary tracks adopted within BOCCE, the best solutions were found for subsolar metallicity ($Z < 0.008$). This is the case in which we were able to obtain a good fit of both V, $B-V$ and V, $V-I$ observational CMDs after adopting the standard extinction law ($E(V-I) = 1.25 \times E(B-V)$, $R_V = 3.1$, see Dean, Warren & Cousins 1978). The interval of confidence of the cluster age turned out to be between 2.9 and 4.0 Gyr (for models without and with overshooting, respectively).

Fig. 9 shows the comparison between the DR-corrected observational CMD inside 3 arcmin from the cluster centre (top left) and the best fits obtained with the three sets of tracks. To better compare data and models we indicated the age sensitive indicators (see Section 2.5) both in the observed and in the synthetic CMDs.

For the Padova models, the set in better agreement with the observational features has metallicity $Z = 0.004$ ([Fe/H] ∼ −0.6 dex). We were able to well reproduce the MS shape, the RH, and MSTP colours and luminosity levels. The age is 4.0 ± 0.2 Gyr. We obtained a slightly redder RGB and RC in the synthetic CMDs (less than 0.1 mag) but the luminosity levels of both RC and BRGB are reproduced. The estimates for reddening and distance modulus for this solution are $E(B-V) = 0.62 \pm 0.04$ mag and $(m-M)_0 = 12.25 \pm 0.1$ mag.

In the case of the FRANEC models the best tracks have $Z = 0.006$ ([Fe/H] ∼ −0.5 dex). We found a general good fit of the luminosity level for the RH, MSTP, BRGB, and RC indicators, but generally a redder colour for RGB and RC (about 0.1 mag). We obtained the best fit for an age of 2.9 ± 0.2 Gyr (models without overshooting always predict smaller age values), a reddening of $E(B-V) = 0.66 \pm 0.04$ mag, and a distance modulus $(m-M)_0 = 12.44 \pm 0.1$ mag.

The best agreement between synthetic and observed CMDs is found with the FST models with moderate overshooting, in terms of the best reproduction of the overall observed CMD morphology. The differences of the synthetic CMDs for $Z = 0.006$ ([Fe/H] ∼ −0.5 dex) are very small. The MS shape is well reproduced as well as the luminosity level of the age sensitive indicators RH, MSTP, BRGB, and RGB. Also in this case the colour of the giant phases are slightly redder but by less than 0.1 mag. The parameter estimates are: age 3.5 ± 0.2 Gyr, $E(B-V) = 0.60 \pm 0.04$ mag, and $(m-M)_0 = 12.35 \pm 0.1$ mag.

Table 9 shows the cluster parameters we derived, together with the implied Galactocentric distance and height. We recall that literature values range between 3 and 6 Gyr for the age, 0.5 and 0.8 mag for the reddening, 10 and 12.6 mag for the distance modulus and there is general agreement on a subsolar metallicity. The differences are mostly due to the methods used by the authors in deriving the parameters. For example, K98 used the morphological parameters ΔV and/or $\Delta(B-V)$, $\Delta(V-I)$ (e.g. Castellani et al. 2000) of the magnitude/colour differences between TO and RC. They estimated an age of 4.1 Gyr but adopting solar metallicity. P04 used a similar method, the δV index – the difference in magnitude between the RC and the TO level (Phelps, Janes & Montgomery 1994) – and the Morphological Age Index calibrated by Janes & Phelps (1994) estimating an age of 4.6 Gyr. However, these methods are weak when one or both the TO or RC phases on the CMD are contaminated by field stars. This is the case of Tr 5: although the RC is evident, the TO is not, even in the inner parts of the cluster. Our method uses at the same time more age sensitive indicators together, hence it is more robust against such uncertainties.

5 SUMMARY AND DISCUSSION

Tr 5 is a populous OC in the anticentre direction. We were able to perform a complete analysis of the cluster properties by combining the information from photometric and spectroscopic observations.

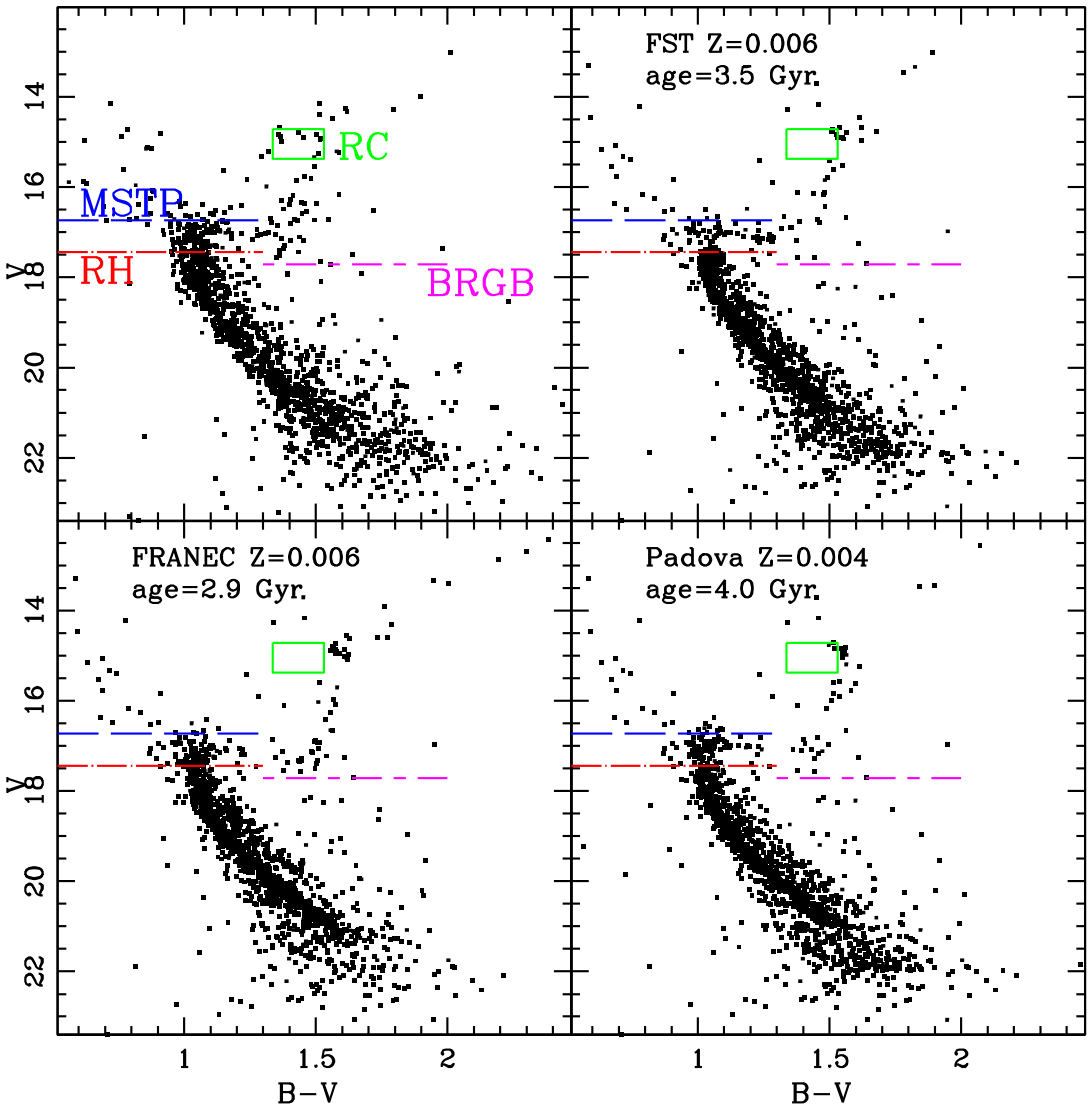

Figure 9. Upper-left panel: DR-corrected observational CMD. The other panels are the synthetic CMDs for the different evolutionary models used and described in this section.

Table 9. Cluster parameters derived using different models. Recall that the spectroscopic metallicity we found is [Fe/H] = −0.4.

Model	Age (Gyr)	Z^a	$(m-M)_0$ (mag)	$E(B-V)$ (mag)	$d_\odot$ (kpc)	$R_{GC}{}^b$ (kpc)	Z (pc)	M_{TO} ($M_\odot$)
Padova	4.0	0.004	12.25	0.62	2.82	10.65	49.9	1.15
FST	3.5	0.006	12.35	0.60	2.95	10.78	52.3	1.24
FRANEC	2.9	0.006	12.44	0.66	3.08	10.90	54.5	1.23

[a]Metal content of the evolutionary tracks.
[b]$R_\odot = 8$ kpc is used to compute R_{GC}.

We obtained a CMD about two mag deeper than the literature ones and on a larger FoV thanks to the WFI instrument. We found that the cluster is located in a region with large DR, and we were able to quantify it within a radius of 4 arcmin. The synthetic CMD technique allowed us to infer the most likely range for age, metallicity, binary fraction, reddening, and distance. We used three different sets of stellar tracks (Padova, FST, FRANEC) to describe the evolutionary status of the cluster in order to take into account how different models impact the accuracy of the analysis. We found that Tr 5 is located at about 3 kpc from the Sun. Its position in the Galactic disc is at $R_{GC} \sim 11$ kpc and 50 pc above the plane (assuming $R_\odot = 8$ kpc). The resulting age is between 2.9 and 4 Gyr, depending on the adopted stellar model, with better fits for ages between 3.5 and 4.0 Gyr. The mean Galactic reddening $E(B-V)$ is between 0.6 and 0.7 mag, and we estimate a fraction of binaries of at least 25 per cent. The photometric metallicity is lower than solar, in the range $0.004 < Z < 0.006$. While this estimation is coarse, the agreement with the spectroscopic analysis is very good.

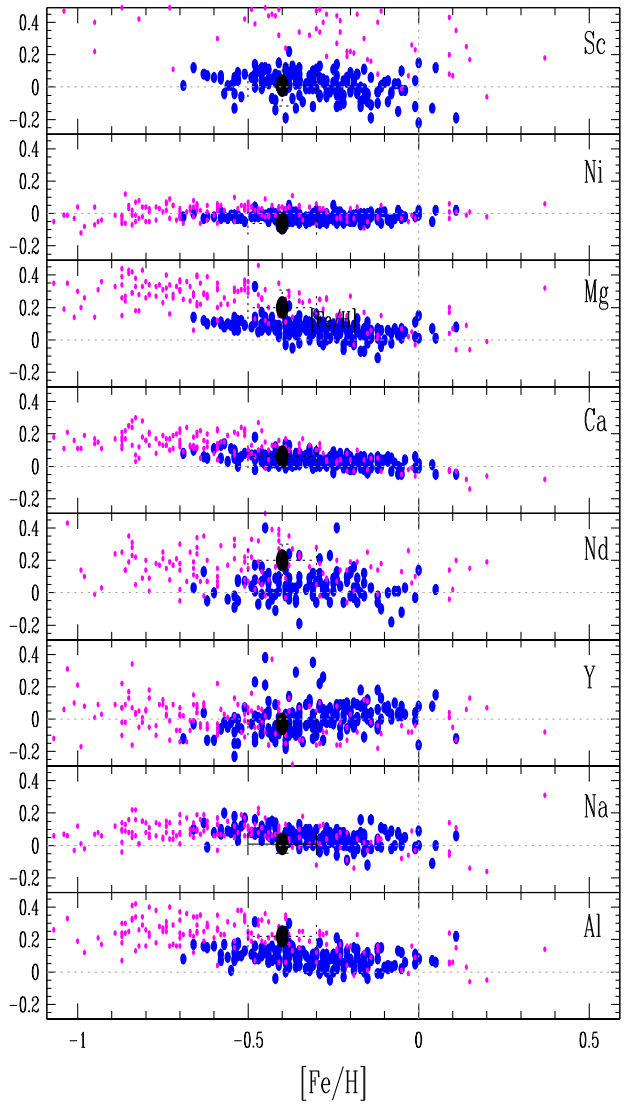

Figure 10. Comparison between the abundances derived for two light elements (Na and Al), two alpha-elements (Mg and Ca), two Fe-peak elements (Sc and Ni), and to heavy elements (Y and Nd) for Tr 5 (black dot) with thin (blue, Reddy et al. 2003) and thick (magenta, Reddy et al. 2006) disc field stars.

From the analysis of the high-resolution UVES spectra of three RC stars we derived an average cluster metallicity [Fe/H] = -0.403 ± 0.006 dex, i.e. with a tiny spread. This was also found by a recent analysis of four other RC stars by Monaco et al. (2014). We also derived abundances of light, α, Fe-group, and n-capture elements. All their ratios to iron appear to be solar with a very small dispersion within the cluster (see Table 8). The abundance ratios we obtained are typical of thin disc star of similar metallicity, as shown also by Fig. 10, where we plot the results for Tr 5 together with those of field disc stars, both of the thin and the thick component (Reddy et al. 2003; Reddy, Lambert & Allende Prieto 2006). In general, the obtained abundances for Tr 5 match those observed in the thin disc. For some chemical species like Mg, Nd, and Al the observed abundance ratios seem more similar to those observed in the thick disc; however, taking into account the error bars, there is no real discrepancy with the thin disc's distribution.

In Fig. 11, we plotted the location of Tr 5 in the R_{GC}, age, and distance from the plane versus [Fe/H]. As comparison we also plotted other OCs in the BOCCE sample using metallicity determined from high-resolution spectroscopy, either by our group or in literature papers. Tr 5 does not show any peculiar property, but it is clearly one of the oldest and most metal-poor OCs. It is located near the Galactocentric distance where the radial metallicity gradient changes slope and flattens (see the upper panel of Fig. 11) where there are other OCs with similar features. This picture is independent of the OCs metallicity source used (see e.g. Heiter et al. 2014). More homogeneous OC metallicities and fundamental parameters will be soon available thanks to the results expected from the *Gaia* satellite and the ongoing large spectroscopic surveys, like APOGEE (Majewski et al. 2010) and the *Gaia*-ESO Survey (Gilmore et al. 2012; Randich et al. 2013), which are targeting many OCs, see e.g. the first results presented by Frinchaboy et al. (2013) for the former and Donati et al. (2014b), Friel et al. (2014) and Magrini et al. (2014) for the latter. Anyway, detailed studies combining photometry, spectroscopy and evolutionary models for particular interesting clusters, like Tr 5, will still be needed in the large surveys era.

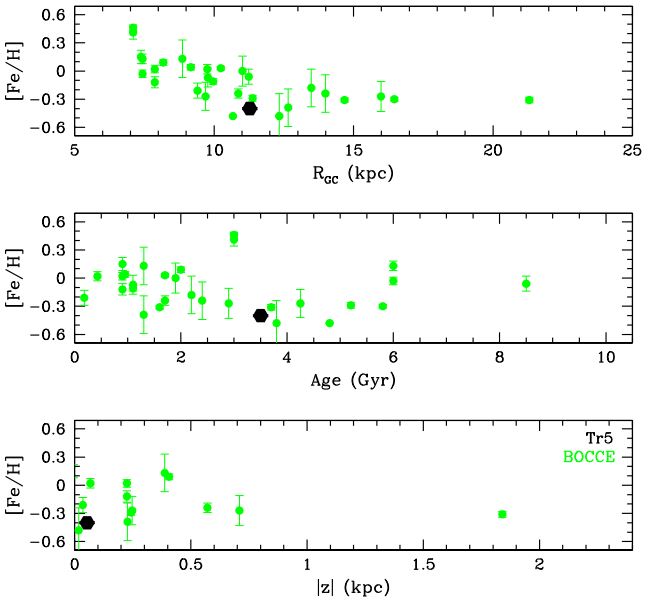

Figure 11. Run of [Fe/H] with R_{GC} (top), age (middle), and $|z|$ (bottom) of the OCs studied by BOCCE (green points). Tr 5 is the black hexagon. Note that the error bars are smaller than the size of the point.

ACKNOWLEDGEMENTS

We thank Paolo Montegriffo (INAF-Osservatorio Astronomico di Bologna, Italy) for his software CataPack, Alessio Mucciarelli for his help with GALA, and Michele Cignoni for useful discussions. This research has made use of National Aeronautics and Space Administration (NASA) Astrophysics Data System, the SIMBAD data base and Aladin (operated at CDS, Strasbourg, France), and the WEBDA data base (originally developed by J.-C. Mermilliod, now operated at the Department of Theoretical Physics and Astrophysics of the Masaryk University, Brno). This research has been partially funded by MIUR and INAF (grants 'The Chemical and Dynamical Evolution of the Milky Way and Local Group Galaxies', prot. 2010LY5N2T; grant 'Premiale VLT 2012'). DSS was produced at the Space Telescope Science Institute under US Government grant NAGW-2166. The images of these surveys are based on photographic data obtained using the Oschin Schmidt Telescope on Palomar Mountain and the UK Schmidt Telescope. The plates were

processed into the present compressed digital form with the permission of these institutions), and the Guide Star Catalogue-II (GSC II is a joint project of the Space Telescope Science Institute) and the Osservatorio Astronomico di Torino. Funding for the SDSS and SDSS-II has been provided by the Alfred P. Sloan Foundation, the Participating Institutions, the National Science Foundation, the US Department of Energy, the NASA, the Japanese Monbukagakusho, the Max Planck Society, and the Higher Education Funding Council for England. The SDSS website is http://www.sdss.org/. The SDSS is managed by the Astrophysical Research Consortium for the Participating Institutions. The Participating Institutions are the American Museum of Natural History, Astrophysical Institute Potsdam, University of Basel, University of Cambridge, Case Western Reserve University, University of Chicago, Drexel University, Fermilab, the Institute for Advanced Study, the Japan Participation Group, Johns Hopkins University, the Joint Institute for Nuclear Astrophysics, the Kavli Institute for Particle Astrophysics and Cosmology, the Korean Scientist Group, the Chinese Academy of Sciences (LAMOST), Los Alamos National Laboratory, the Max-Planck-Institute for Astronomy (MPIA), the Max-Planck-Institute for Astrophysics (MPA), New Mexico State University, Ohio State University, University of Pittsburgh, University of Portsmouth, Princeton University, the United States Naval Observatory, and the University of Washington.

REFERENCES

Ahumada A. V., Cignoni M., Bragaglia A., Donati P., Tosi M., Marconi G., 2013, MNRAS, 430, 221
Bessell M. S., Castelli F., Plez B., 1998, A&A, 333, 231
Bonnarel F. et al., 2000, A&AS, 143, 33
Bragaglia A., Tosi M., 2006, AJ, 131, 1544
Bragaglia A., Sestito P., Villanova S., Carretta E., Randich S., Tosi M., 2008, A&A, 480, 79
Bressan A., Fagotto F., Bertelli G., Chiosi C., 1993, A&AS, 100, 647
Brogaard K. et al., 2012, A&A, 543, A106
Cantat-Gaudin T. et al., 2014, A&A, 562, A10
Carrera R., Pancino E., 2011, A&A, 535, A30
Carrera R., Gallart C., Pancino E., Zinn R., 2007, AJ, 134, 1298
Castellani V., Degl'Innocenti S., Girardi L., Marconi M., Prada Moroni P. G., Weiss A., 2000, A&A, 354, 150
Castelli F., Kurucz R. L., 2003, in Piskunov N., Weiss W. W., Gray D. F., eds, Proc. IAU Symp. 210, Modelling of Stellar Atmospheres. Astron. Soc. Pac., San Francisco, p. 20
Cayrel R. et al., 2004, A&A, 416, 1117
Cignoni M., Beccari G., Bragaglia A., Tosi M., 2011, MNRAS, 416, 1077
Cole A. A., Smecker-Hane T. A., Tolstoy E., Bosler T. L., Gallagher J. S., 2004, MNRAS, 347, 367
D'Odorico S., Cristiani S., Dekker H., Hill V., Kaufer A., Kim T., Primas F., 2000, Proc. SPIE, 4005, 121
Dean J. F., Warren P. R., Cousins A. W. J., 1978, MNRAS, 183, 569
Dias W. S., Alessi B. S., Moitinho A., Lépine J. R. D., 2002, A&A, 389, 871
Dominguez I., Chieffi A., Limongi M., Straniero O., 1999, ApJ, 524, 226
Donati P., Bragaglia A., Cignoni M., Cocozza G., Tosi M., 2012, MNRAS, 424, 1132
Donati P., Beccari G., Bragaglia A., Cignoni M., Tosi M., 2014a, MNRAS, 437, 1241
Donati P. et al., 2014b, A&A, 561, A94
Dow M. J., Hawarden T. G., 1970, Mon. Notes Astron. Soc. South. Afr., 29, 137
Fagotto F., Bressan A., Bertelli G., Chiosi C., 1994, A&AS, 105, 29
Friel E. D., 1995, ARA&A, 33, 381
Friel E. D. et al., 2014, A&A, 563, A117
Frinchaboy P. M. et al., 2013, ApJ, 777, L1
Gilmore G. et al., 2012, The Messenger, 147, 25
Grevesse N., Noels A., Sauval A. J., 1996, in Holt S. S., Sonneborn G., eds, ASP Conf. Ser. Vol. 99, Standard Abundances. Astron. Soc. Pac., San Francisco, p. 117
Gustafsson B., Edvardsson B., Eriksson K., Jørgensen U. G., Nordlund Å., Plez B., 2008, A&A, 486, 951
Heiter U., Soubiran C., Netopil M., Paunzen E., 2014, A&A, 561, A93
Janes K. A., Phelps R. L., 1994, AJ, 108, 1773
Kaluzny J., 1998, A&AS, 133, 25 (K98)
Kim S. C., Sung H., 2003, J. Korean Astron. Soc., 36, 13
Kim S. C., Kyeong J., Sung E.-C., 2009, J. Korean Astron. Soc., 42, 135
Koch A., Odenkirchen M., Caldwell J. A. R., Grebel E. K., 2003, ANS, 324, 95
Kurucz R. L., 2005, Mem. Soc. Astron. Ital. Suppl., 8, 14
Landolt A., 1992, AJ, 104, 340
Lépine J. R. D. et al., 2011, MNRAS, 417, 698
Magrini L., Sestito P., Randich S., Galli D., 2009, A&A, 494, 95
Magrini L. et al., 2014, A&A, 563, A44
Majewski S. R., Wilson J. C., Hearty F., Schiavon R. R., Skrutskie M. F., 2010, in Cunha K., Spite M., Barbuy B., eds, Proc. IAU Symp. 265, Chemical Abundances in the Universe: Connecting First Stars to Planets. Cambridge Univ. Press, Cambridge, p. 480
Milone A. P. et al., 2012, A&A, 540, A16
Monaco L. et al., 2014, A&A, 564, L6
Mucciarelli A., Pancino E., Lovisi L., Ferraro F. R., Lapenna E., 2013, ApJ, 766, 78
Pancino E., Carrera R., Rossetti E., Gallart C., 2010, A&A, 511, A56
Phelps R. L., Janes K. A., Montgomery K. A., 1994, AJ, 107, 1079
Piatti A. E., Clariá J. J., Ahumada A. V., 2004, MNRAS, 349, 641 (P04)
Platais I. et al., 2012, ApJ, 751, L8
Randich S., Gilmore G., Gaia-ESO Consortium, 2013, The Messenger, 154, 47
Reddy B. E., Tomkin J., Lambert D. L., Allende Prieto C., 2003, MNRAS, 340, 304
Reddy B. E., Lambert D. L., Allende Prieto C., 2006, MNRAS, 367, 1329
Ryabchikova T. A., Pakhomov Y. V., Piskunov N. E., 2011, Kazan Izdatel Kazanskogo Univ., 153, 61
Sbordone L., Bonifacio P., Castelli F., Kurucz R. L., 2004, Mem. Soc. Astron. Ital. Suppl., 5, 93
Sestito P., Bragaglia A., Randich S., Pallavicini R., Andrievsky S. M., Korotin S. A., 2008, A&A, 488, 943
Skrutskie M. F. et al., 2006, AJ, 131, 1163
Stetson P. B., 1987, PASP, 99, 191
Stetson P. B., 1993, in Butler C. J., Elliott I., eds, Proc. IAU Colloq. 136: Stellar Photometry - Current Techniques and Future Developments. Cambridge Univ. Press, Cambridge, p. 291
Stetson P. B., Pancino E., 2008, PASP, 120, 1332
Tosi M., Greggio L., Marconi G., Focardi P., 1991, AJ, 102, 951
Ventura P., Zeppieri A., Mazzitelli I., D'Antona F., 1998, A&A, 334, 953
Yong D., Carney B. W., Friel E. D., 2012, AJ, 144, 95

SUPPORTING INFORMATION

Additional Supporting Information may be found in the online version of this article:

Table 7. Equivalent widths of the used atomic species (http://mnras.oxfordjournals.org/lookup/suppl/doi:10.1093/mnras/stu2162/-/DC1).

Please note: Oxford University Press is not responsible for the content or functionality of any supporting materials supplied by the authors. Any queries (other than missing material) should be directed to the corresponding author for the paper.

This paper has been typeset from a TEX/LATEX file prepared by the author.